Microscopic temperature field prediction during adiabatic loading using gradient extended crystal plasticity
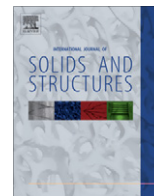
(article starts on next page)

Microscopic temperature field prediction during adiabatic loading using gradient extended crystal plasticity

Swantje Bargmann [a], Magnus Ekh [b],*

[a] Institute of Continuum Mechanics and Material Mechanics, TU Hamburg-Harburg & Helmholtz-Zentrum Geesthacht, Institute of Materials Research, Geesthacht, Germany
[b] Division of Material and Computational Mechanics, Department of Applied Mechanics, Chalmers University of Technology, Gothenburg, Sweden

ABSTRACT

The problem of interest is grain-size-dependent hardening in polycrystalline metals. We study the multiphysics problem of heat conduction coupled to gradient crystal plasticity and investigate the temperature field on the grain level for adiabatic loading. The underlying equations for the thermomechanical coupling are derived for a crystal plasticity model with gradient hardening. The influence of the temperature field on misorientation of the slip directions between adjacent grains is investigated. Additionally, the influence of the loading velocity and the size of the grain structure are examined. Numerical simulations are presented and analyzed.

© 2012 Elsevier Ltd. All rights reserved.

1. Introduction

Due to the increasing significance of newly developed materials and/or materials with improved properties, materials characterization and simulation become more and more powerful tools and important. In this contribution, we focus on microstructured solids undergoing forming processes. Rapid processing is important for the competitiveness of the industry. Examples of rapid processing are adiabatic cutting and adiabatic forming. The heating in thin regions with localized plastic deformation and the followed material softening explains how the adiabatic process can work. We aim at increasing the understanding the initiation of these phenomena on the grain level of metals ($\sim\mu m$).

To model the material behavior at the grain level crystal plasticity is a well-established tool (see e.g., Hill, 1966; Rice, 1971; Asaro, 1983). The crystal plasticity models have been extended to gradient crystal plasticity models in order to capture grain size dependence (see e.g., Gurtin, 2000; Cermelli and Gurtin, 2001; Evers et al., 2004; Anand et al., 2005; Ekh et al., 2007; Svendsen and Bargmann, 2010). The physical motivation for including gradient effects is that movement of dislocations (plastic slip) is affected by the grain boundaries in a polycrystal. In the present paper we will investigate how the thermal field on the grain level will be affected by grain boundaries using an extended version of the crystal gradient plasticity model proposed in Ekh et al. (2007). There exist some contributions taking a temperature-dependent initial yield

stress into account, however, without modeling heat conduction inside the material (cf. e.g., Evers et al., 2004; Nemat-Nasser et al., 2001; Voyiadjis and Beliktas, 2005). Lately, Al-Rub and Faruk (2011) studied temperature effects on size-dependent yield strength and strain hardening of small metallic volumes.

The framework for consistently deriving the heat generation due to dissipation of a crystal plasticity model was formulated by Håkansson et al. (2008). In Håkansson et al. (2008) crystal plasticity was used to model the macroscopic heat generation of a polycrystal using a Taylor assumption for the displacement field on the grain level. However, in the current paper we will on the grain level allow for a fluctuating displacement and temperature field. The fluctuation of the temperature field is of significance in application areas such as rapid processing or for large grain size of the polycrystal such as superalloys.

Most works devoted to gradient extended crystal plasticity only deal with the mechanical issue (which is challenging enough). However, thermal effects play a non-negligible role in different cases and should therefore be taken into account. In general, for slow as well as for rapid strain rates the stress–strain response depends on the local temperature (e.g., Nemat-Nasser et al., 2001; Zhou and Clode, 1998).

One example is that, in context of macro- as well as microforming processes, the material's temperature slightly decreases before the yield point and increases when yielding starts. The temperature change between the drop and the increase is a relatively sharp kink, whereas the temperature rise is linear afterwards. In forming technology it is still an unresolved issue on how the temperature influences the exact determination of the yielding point. During

* Corresponding author. Tel.: +46 31 7723479.
   E-mail address: magnus.ekh@chalmers.se (M. Ekh).

the forming process, the temperature of the specimen rises due to heat generated by plastic deformation. Another example is the interaction of temperature and microstructure in the other direction, i.e., the microstructure influences thermal properties: grain boundaries decrease the thermal (and the electrical) conductivity, depending on the number of misfit dislocations.

The numerical algorithm chosen in this paper, for the gradient plasticity, is based on the dual mixed method proposed in Svedberg and Runesson (1998) and applied in Ekh et al. (2007) for a gradient crystal plasticity model. Further, in Ekh et al. (2007) the grain structure is numerically divided into grains (domain decomposition) and the field problems (displacement and gradient of plastic slip) are solved for in each grain separately for given displacements at the grain boundaries. The global field problem is then reduced to finding the displacements on the grain boundaries. In the current paper this algorithm has been extended to together with the displacement field also solve for the temperature field in a monolithic fashion.

The paper is organized as follows: in Section 2 the notation and the kinematics are introduced. The governing equations are derived in a thermodynamically consistent fashion from fundamental balance principles in Section 3. The restrictions that arise from the reduced dissipation inequality stipulate the thermodynamically consistent form of the constitutive equations. This framework is then utilized to determine the response of the polycrystal in Section 4. The numerical solution algorithm is described in Section 5. The theory is implemented into a two-dimensional finite element code. This is done within the context of a dual-mixed finite element method. Section 6 is devoted to the boundary conditions of the problem at hand. Finally, some numerical examples are discussed in Section 7 and, subsequently, Section 8 concludes this contribution.

2. Kinematics

The motion of particles X in the reference configuration $\mathcal{B}_0$ of the solid body with boundary Γ_0 is described by the time-dependent vector field of the nonlinear spatial deformation map

$$\varphi : \mathcal{B}_0 \times \mathbb{R}_+ \to \mathcal{B}_t \quad \text{with} \quad \varphi(X,t) := x, \tag{1}$$

where x denotes the spatial position of the particle X in the deformed (spatial) configuration $\mathcal{B}_t$ at time t. The body $\mathcal{B}_0$ consists of several grains. The boundary of each grain is denoted by $\Gamma_{\beta,\text{grain}}$, see also Fig. 1.

The deformation gradient F is defined by

$$F : \mathcal{T}\mathcal{B}_0 \to \mathcal{T}\mathcal{B}_t \quad \text{with} \quad F := \nabla_0 \varphi(X,t). \tag{2}$$

The I-th component of the nabla operator is defined as $\nabla_0(\bullet)_I = \partial(\bullet)/\partial X_I$. The deformation gradient is assumed to be multiplicatively split into an elastic F^e (reversible) and a a plastic (irreversible) part F^p:

$$F = F^e \cdot F^p, \tag{3}$$

see e.g., Kröner (1960), Lee (1969). The Jacobian of the deformation gradient is denoted $J = \det F$. Useful deformation measures are the right Cauchy–Green and Finger tensors which are defined as follows

$$C := F^t \cdot F, \quad C^e := [F^e]^t \cdot F^e, \quad b^e := F^e \cdot [F^e]^t. \tag{4}$$

Moreover, we make use of the velocity gradient l which can be expressed as follows by using the multiplicative split of the deformation gradient

$$l := \dot{F} \cdot F^{-1} = l^e + l^p \tag{5}$$
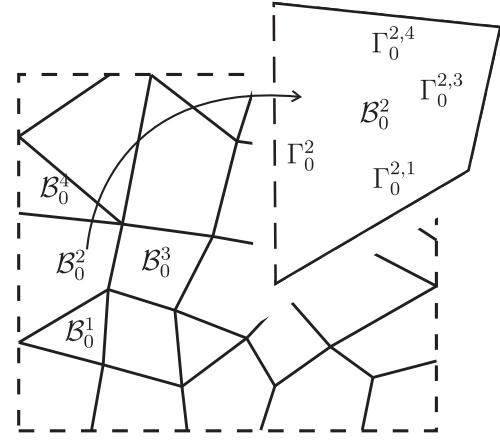
with

Fig. 1. We consider a polycrystal with domain $\mathcal{B}_0$ which consists of multiple grains. Each grain β occupies a domain $\mathcal{B}_{0,\text{grain}\beta}$ with $\mathcal{B}_0 = \bigcup_\beta \mathcal{B}_{0,\text{grain}\beta}$. To the specimen's boundary (i.e., the dashed line) we refer as the outer boundary. Those grain boundaries $\Gamma_{0,\text{grain}\beta}$ which are not part of the outer boundary we name inner boundaries (i.e., all solid lines). For example, $\Gamma_{0,\text{grain}2}$ is an outer boundary, while $\Gamma_{0,\text{grain}2,1}$, $\Gamma_{0,\text{grain}2,3}$ and $\Gamma_{0,\text{grain}2,4}$ are inner boundaries.

$$l^e := \dot{F}^e \cdot [F^e]^{-1}, \quad l^p := F^e \cdot \dot{F}^p \cdot [F^p]^{-1} \cdot [F^e]^{-1}. \tag{6}$$

The rate of deformation tensor d which is defined as the symmetric part of the velocity gradient, i.e.,

$$d := \frac{1}{2}\left[l + l^t\right]. \tag{7}$$

Clearly, then the rate of deformation tensor can also be additively decomposed as $d = d^e + d^p$ where both d^e and d^p are the symmetrictively decomposed as $d = d^e + d^p$ where both d^e and d^p are the symmetric part of the corresponding velocity gradients l^e and l^p. Finally, a result that we need later is the time derivative of the elastic Cauchy-Green deformation C^e that can be written as

$$\dot{C}^e = 2[F^e]^t \cdot d^e \cdot F^e. \tag{8}$$

3. Thermodynamic framework

The first law of thermodynamics states the conservation of total energy, in terms of balance equations this is also referred to as the balance of energy. We assume conservation of mass and make use of the balance of momentum

$$\rho_0 \dot{v} = \text{Div}\, P + \rho_0 b, \tag{9}$$

with P and b being the first Piola–Kirchhoff stress tensor and the volume force, respectively. The divergence operator is defined as $\text{Div}(\bullet) = \sum_I \partial(\bullet)/\partial X_I$. Then, the first law reduces to the balance of internal energy in its conservative form

$$\int_{\mathcal{B}_0} \rho_0 \dot{\varepsilon}\, dV = -\int_{\mathcal{B}_0} \text{Div}\, Q\, dV + \int_{\mathcal{B}_0} P : \dot{F}\, dV + \int_{\mathcal{B}_0} \rho_0 r\, dV, \tag{10}$$

where ε is the mass specific internal energy density, r is the external heat supply per unit mass and Q is the material heat flux vector. The spatial counterparts of the first Piola–Kirchhoff stress P and the heat flux Q are obtained via the Piola transformations

$$\sigma = J^{-1} P \cdot F^t, \quad q = J^{-1} Q \cdot F^t, \tag{11}$$

where σ is the Cauchy stress and q is the spatial heat flux.

The point of departure, for formulating a constitutive model, is the entropy inequality in combination with the second law of ther-

modynamics which ensure the non-negativity of the internal entropy production:

$$\int_{\mathcal{B}_0} \rho_0 \dot{\eta} dV - \int_{\mathcal{B}_0} \rho_0 r/\theta dV + \int_{\mathcal{B}_0} \text{Div}(\boldsymbol{Q}/\theta) dV \geqslant 0, \tag{12}$$

where η denotes the entropy density and θ is the absolute temperature. Inserting the definition of the Helmholtz free energy $\psi := \varepsilon - \eta\theta$ and subsequently balance equation (10) into Eq. (12) leads to

$$\int_{\mathcal{B}_0} \boldsymbol{P} : \dot{\boldsymbol{F}} dV - \int_{\mathcal{B}_0} \rho_0 \dot{\psi} dV - \int_{\mathcal{B}_0} \rho_0 \eta \dot{\theta} dV - \int_{\mathcal{B}_0} \nabla_0 \theta \cdot \frac{\boldsymbol{Q}}{\theta} dV \geqslant 0. \tag{13}$$

The framework is complemented by constitutive equations which are introduced in Section 4. At this point, we assume that the following independent variables define the state space $\mathbb{S}$: the elastic Cauchy-Green deformation tensor $\boldsymbol{C}^e$, the hardening variables $\boldsymbol{v} = (v_1, \ldots, v_{n_{\text{slip}}})$, the gradients of the hardening variables $\nabla_0 \boldsymbol{v} = (\nabla_0 v_1, \ldots, \nabla_0 v_{n_{\text{slip}}})$ and the (absolute) temperature θ. Thus, the Helmholtz free energy ψ depends on the state space $\mathbb{S} = \{\boldsymbol{C}^e, \boldsymbol{v}, \nabla_0 \boldsymbol{v}, \theta\}$ and we obtain $\psi = \psi(\boldsymbol{C}^e, \boldsymbol{v}, \nabla_0 \boldsymbol{v}, \theta)$. Next, we insert this assumption into Eq. (13), rearrange and make use of the fact that inequality (12) must hold for all thermodynamical processes. This motivates the following constitutive assumptions:

$$\eta = -\frac{\partial \psi}{\partial \theta}, \quad \boldsymbol{\tau} = 2\rho_0 \boldsymbol{F}^e \cdot \frac{\partial \psi}{\partial \boldsymbol{C}^e} \cdot [\boldsymbol{F}^e]^t, \tag{14}$$

where $\boldsymbol{\tau} := J\boldsymbol{\sigma}$ is the Kirchhoff stress. In addition, we obtain the reduced dissipation inequality:

$$\mathcal{D} := \int_{\mathcal{B}_{0,\text{grain}}} \boldsymbol{\tau} : \boldsymbol{d}^p - \frac{\rho_0 \partial \psi}{\partial \boldsymbol{v}} \cdot \dot{\boldsymbol{v}} - \frac{\rho_0 \partial \psi}{\partial \nabla_0 \boldsymbol{v}} : \nabla_0 \dot{\boldsymbol{v}} - \nabla_0 \theta \cdot \frac{\boldsymbol{Q}}{\theta} dV$$
$$\geqslant 0. \tag{15}$$

We split the total dissipation $\mathcal{D} = \mathcal{D}_{\text{mech}} + \mathcal{D}_{\text{therm}} \geqslant 0$ into a mechanical and a thermal contribution

$$\mathcal{D}_{\text{mech}} = \int_{\mathcal{B}_{0,\text{grain}}} \boldsymbol{\tau} : \boldsymbol{d}^p + \boldsymbol{\kappa} \cdot \dot{\boldsymbol{v}} dV + \int_{\Gamma_{0,\text{grain}}} \boldsymbol{\kappa}^{(b)} \cdot \dot{\boldsymbol{v}} dA,$$
$$\mathcal{D}_{\text{therm}} = -\int_{\mathcal{B}_{0,\text{grain}}} \frac{1}{\theta} \boldsymbol{Q} \cdot \nabla_0 \theta dV, \tag{16}$$

where we introduced the microstresses $\boldsymbol{\kappa} = (\kappa_1, \ldots, \kappa_{n_{\text{slip}}})$ and $\boldsymbol{\kappa}^{(b)} = (\kappa_1^{(b)}, \ldots, \kappa_{n_{\text{slip}}}^{(b)})$ as follows

$$\kappa_\beta = -\frac{\rho_0 \partial \psi}{\partial v_\beta} + \text{Div}\left(\frac{\rho_0 \partial \psi}{\partial \nabla_0 v_\beta}\right) \quad \text{in } \mathcal{B}_{0,\text{grain}},$$

$$\kappa_\beta^{(b)} = -\boldsymbol{N} \cdot \frac{\rho_0 \partial \psi}{\partial \nabla_0 v_\beta} \quad \text{on } \Gamma_{0,\text{grain}}, \tag{17}$$

with $\beta = 1, 2, \ldots, n_{\text{slip}}$. Note that the microstress inside the grain as well as on the boundary naturally arise from the theory. In particular, the later motivates the micro boundary conditions. Both dissipations $\mathcal{D}_{\text{mech}}$ and $\mathcal{D}_{\text{therm}}$ have to be non-negative. The mechanical dissipation $\mathcal{D}_{\text{mech}}$ can be rephrased as

$$\mathcal{D}_{\text{mech}} = \int_{\mathcal{B}_{0,\text{grain}}} \boldsymbol{M} : \boldsymbol{L}^p + \boldsymbol{\kappa} \cdot \dot{\boldsymbol{v}} dV + \int_{\Gamma_{0,\text{grain}}} \boldsymbol{\kappa}^{(b)} \cdot \dot{\boldsymbol{v}} dA \tag{18}$$

by introducing the Mandel stress

$$\boldsymbol{M} = 2\boldsymbol{C}^e \cdot \frac{\rho_0 \partial \psi}{\partial \boldsymbol{C}^e} \tag{19}$$

and the plastic velocity gradient (on the intermediate tangent space)

$$\boldsymbol{L}^p = \dot{\boldsymbol{F}}^p \cdot [\boldsymbol{F}^p]^{-1}. \tag{20}$$

Next, we aim at deriving the governing equation for the thermal problem. We insert the definition of the Helmholtz free energy and subsequently relations (14) and (18) into balance equation (10). In each grain $\mathcal{B}_{0,\text{grain}}$ we obtain

$$\int_{\mathcal{B}_{0,\text{grain}}} \rho_0 c \dot{\theta} dV = \int_{\mathcal{B}_{0,\text{grain}}} -\text{Div}\boldsymbol{Q} + \rho_0 r dV + \mathcal{D}_{\text{mech}}$$
$$+ \int_{\mathcal{B}_{0,\text{grain}}} \rho_0 \theta \left[\frac{\partial^2 \psi}{\partial\theta\partial\boldsymbol{C}^e} : \dot{\boldsymbol{C}}^e + \frac{\partial^2 \psi}{\partial\theta\partial\boldsymbol{v}} \cdot \dot{\boldsymbol{v}} + \frac{\partial^2 \psi}{\partial\theta\partial\nabla_0\boldsymbol{v}} : \nabla_0 \dot{\boldsymbol{v}}\right] dV. \tag{21}$$

Here, $c = -\theta \partial^2 \psi / \partial \theta^2$ denotes the non-negative specific heat. Next, we apply the divergence theorem and theorem of Gauss which leads to

$$\int_{\mathcal{B}_{0,\text{grain}}} \rho_0 c \dot{\theta} dV = \int_{\mathcal{B}_{0,\text{grain}}} -\text{Div}\boldsymbol{Q} + \rho_0 r dV + \mathcal{D}_{\text{mech}}$$
$$+ \int_{\mathcal{B}_{0,\text{grain}}} \rho_0 \theta \frac{\partial^2 \psi}{\partial\theta\partial\boldsymbol{C}^e} : \dot{\boldsymbol{C}}^e dV$$
$$+ \int_{\mathcal{B}_{0,\text{grain}}} \rho_0 \theta \left[\left(\frac{\partial^2 \psi}{\partial\theta\partial\boldsymbol{v}} - \text{Div}\left(\frac{\partial^2 \psi}{\partial\theta\partial\nabla_0\boldsymbol{v}}\right)\right)\dot{\boldsymbol{v}}\right] dV$$
$$+ \int_{\Gamma_{0,\text{grain}}} \frac{\partial^2 \psi}{\partial\theta\partial\nabla_0\boldsymbol{v}} \cdot \boldsymbol{N} \cdot \dot{\boldsymbol{v}} dA. \tag{22}$$

4. Constitutive assumptions

From now on, we assume the following free energy ψ of the Neo–Hookean type

$$\rho_0 \psi := \frac{\mu}{2}\left[\boldsymbol{C}^e - \boldsymbol{I}\right] : \boldsymbol{I} + \frac{\lambda}{2}\ln^2 J - \mu \ln J + \frac{1}{2}\sum_{\beta,\iota}H_{\beta\iota}^l v_\beta v_\iota$$
$$+ \frac{1}{2}\sum_{\beta,\iota}l_\beta l_\iota \nabla_0 v_\beta \cdot \boldsymbol{H}_{\beta\iota}^g \cdot \nabla_0 v_\iota + \rho_0 c\left[\theta - \theta_0 - \theta \ln\frac{\theta}{\theta_0}\right]$$
$$- 3\alpha[\lambda + 2/3\mu][\theta - \theta_0]\frac{\ln J}{J} \tag{23}$$

with λ and μ denoting the Lamé constants and α is the thermal expansion coefficient. Moreover, c and θ_0 denote the non-negative specific heat and the reference temperature, respectively. Furthermore, $H_{\beta\iota}^l$ denotes the local hardening modulus and l_β and l_ι are internal length scales. Moreover, the counterpart for the gradient contribution, i.e., $\boldsymbol{H}_{\beta\iota}^g$, accounts for cross-hardening effects as well:

$$\boldsymbol{H}_{\beta\iota}^g := [\bar{\boldsymbol{s}}_\beta \otimes \bar{\boldsymbol{s}}_\iota]h_{\beta\iota}H_0^g, \tag{24}$$

with H_0^g being the gradient hardening modulus and $\bar{\boldsymbol{s}}_\beta, \bar{\boldsymbol{s}}_\iota$ are slip directions. $h_{\beta\iota}$ are coefficients where the diagonal terms ($\beta = \iota$) are related to gradient self-hardening of the slip systems β, whereas the off-diagonal elements ($\beta \neq \iota$) induce gradient latent hardening between the slip systems β and ι. For now, we assume that both, $H_{\beta\iota}^l$ and $\boldsymbol{H}_{\beta\iota}^g$, are temperature independent.

The choice of Helmholtz' free energy in Eq. (23) results in

$$\boldsymbol{\tau} = \mu[\boldsymbol{b}^e - \boldsymbol{I}] + \lambda \ln(J)\boldsymbol{I} - 3\alpha[\lambda + \frac{2}{3}\mu][\theta - \theta_0][1 - \ln(J)]\frac{\boldsymbol{I}}{J},$$
$$\boldsymbol{M} = \mu[\boldsymbol{C}^e - \boldsymbol{I}] + \lambda \ln(J)\boldsymbol{I} - 3\alpha[\lambda + \frac{2}{3}\mu][\theta - \theta_0][1 - \ln(J)]\frac{\boldsymbol{I}}{J},$$
$$\kappa_\beta = -\sum_\iota H_{\beta\iota}^l v_\iota + \sum_\iota l_\beta H_{\beta\iota}^g l_\iota \text{Div}(\bar{\boldsymbol{s}}_\beta \nabla_0 v_\iota \cdot \bar{\boldsymbol{s}}_\iota),$$
$$\kappa_\beta^{(b)} = -\sum_\iota l_\beta H_{\beta\iota}^g l_\iota \boldsymbol{N} \cdot [\boldsymbol{s}_\beta \nabla_0 v_\iota \cdot \boldsymbol{s}_\iota], \tag{25}$$

when combining Eqs. (14), (17) and (19). For the heat flux $\boldsymbol{Q}$ we assume Fourier's classical law of heat conduction

$$\boldsymbol{Q} := -k\nabla_0\theta \qquad (26)$$

with k denoting the material's thermal conductivity. We adopt the standard crystal plasticity yield function on each slip system β as

$$\Phi_\beta := \tau_\beta - \kappa_\beta - Y_\beta, \qquad (27)$$

where τ_β is the Schmid stress defined as the projection of the Kirchhoff stress $\boldsymbol{\tau}$ on the crystal system

$$\tau_\beta := \boldsymbol{s}_\beta \cdot \boldsymbol{\tau} \cdot \boldsymbol{n}_\beta. \qquad (28)$$

The vectors $\boldsymbol{s}_\beta$ and $\boldsymbol{n}_\beta$ are the slip direction and the normal of the slip plane, respectively. The Schmid stress can also be expressed in quantities defined on the intermediate tangent space as

$$\tau_\beta = \bar{\boldsymbol{s}}_\beta \cdot \boldsymbol{M} \cdot \bar{\boldsymbol{n}}_\beta \qquad (29)$$

with $\bar{\boldsymbol{s}}_\beta$ and $\bar{\boldsymbol{n}}_\beta$ defined from the pull-back operations

$$\bar{\boldsymbol{s}}_\beta = [\boldsymbol{F}^e]^{-1} \cdot \boldsymbol{s}_\beta \quad \text{and} \quad \bar{\boldsymbol{n}}_\beta = \boldsymbol{n}_\beta \cdot \boldsymbol{F}^e. \qquad (30)$$

Note that we adopt the isoclinic assumption that the slip directions on the intermediate and the reference configurations coincide. The evolution equations for the internal variables are defined in an associative fashion as

$$\boldsymbol{L}^p = \sum_{\beta=1}^{n_{slip}} \dot{\gamma}_\beta \frac{\partial \Phi_\beta}{\partial \boldsymbol{M}} = \sum_{\beta=1}^{n_{slip}} \dot{\gamma}_\beta [\bar{\boldsymbol{s}}_\beta \otimes \bar{\boldsymbol{n}}_\beta],$$

$$\dot{v}_\beta = \dot{\gamma}_\beta \frac{\partial \Phi_\beta}{\partial \kappa_\beta} = -\dot{\gamma}_\beta. \qquad (31)$$

Finally, we assume that the slip rate $\dot{\gamma}_\beta$ is governed by a viscoplastic hardening law via a Perzyna-type regularization

$$\dot{\gamma}_\beta = \frac{1}{t_\star} \frac{\langle \tau_\beta - \kappa_\beta - Y_\beta \rangle^m}{C_0}, \qquad (32)$$

where $\langle x \rangle = 1/2[x + |x|]$. The drag stress, the relaxation time and the constant rate sensitivity are denoted C_0, $t_\star$, m, respectively. At this point, C_0 and $t_\star$ are chosen to be constant for the sake of clarity. However, they might as well depend on the temperature and/or on the slip system β.

5. Finite element algorithm

A finite element method is applied to numerically solve the highly nonlinear and coupled boundary value problem: the linear momentum equation (9), the transient heat equation (22) and the gradient problem (32). Following our earlier works on isothermal gradient crystal plasticity (Ekh et al., 2007; Bargmann et al., 2011), we introduce the gradient of the plastic slip along the slip direction g_β as a field variable

$$g_\beta := \nabla_0 \gamma_\beta \cdot \boldsymbol{s}_\beta. \qquad (33)$$

In spirit of the dual mixed finite element algorithm, we solve for the temperature θ, the mechanical displacement $\boldsymbol{u}$ and the directional gradient g_β. The plastic slip γ_β is treated as a dependent variable and solved on the local element level. The time interval of interest is discretized with a backward Euler scheme and we denote quantities at time t_n with a superindex $^n(\bullet)$ while quantities at time t_{n+1} is for convenience written without any superindex. Before proceeding to the FE equations, we summarize the underlying time discretized field equations

$$\rho_0 c \frac{\theta - {}^n\theta}{\Delta t} = k \, \text{Div}(\nabla_0 \theta) + \boldsymbol{\tau} : \boldsymbol{d}^p + \boldsymbol{\kappa} \cdot \dot{\boldsymbol{v}} + \theta \frac{1}{2} \frac{\partial \boldsymbol{S}^e}{\partial \theta} : \dot{\boldsymbol{C}}^e + \theta \frac{\partial \boldsymbol{\kappa}}{\partial \theta} \cdot \dot{\boldsymbol{v}}, \qquad (34)$$

$$\rho_0 \dot{\boldsymbol{v}} = \text{Div} \, \boldsymbol{P} + \rho_0 \boldsymbol{b}, \qquad (35)$$

$$g_\beta = \nabla_0 \gamma_\beta \cdot \boldsymbol{s}_\beta. \qquad (36)$$

Note that we used the localized version of Eq. (22) that can be obtained by disregarding the boundary contributions. The motivation for this is given in the next section where boundary conditions for the plastic slip field γ_β are introduced. Next, the domain is decomposed, i.e., the grain structure is numerically divided into grains (domains), see also Fig. 1. The unknowns are solved for in a staggered iterative fashion on two levels: on the outer level we iterate for the unknowns on all grain boundary nodes inside the specimen (given the values at the outer boundary); for each iteration step on the outer level, the field variables are solved for in each grain (for fixed values at all grain boundaries). The plastic slip γ_β is calculated on the element level in the Gauß points.

In the numerical examples we assume a quasistatic balance of momentum whereby the weak form of these equations become

$$\int_{\mathcal{B}_{0,grain}} \rho_0 c \frac{\theta - {}^n\theta}{\Delta t} \delta\theta \mathrm{d}V = \int_{\Gamma_{0,grain}} k\nabla_0\theta \cdot \boldsymbol{N}\delta\theta \mathrm{d}A - \int_{\mathcal{B}_{0,grain}} k\nabla_0\theta \cdot \nabla_0(\delta\theta)\mathrm{d}V$$
$$+ \int_{\mathcal{B}_{0,grain}} \left[\boldsymbol{\tau} : \boldsymbol{d}^p + \boldsymbol{\kappa} \cdot \dot{\boldsymbol{v}} + \theta \frac{1}{2}\frac{\partial \boldsymbol{S}^e}{\partial\theta} : \dot{\boldsymbol{C}}^e + \theta\frac{\partial\boldsymbol{\kappa}}{\partial\theta}\cdot\dot{\boldsymbol{v}} \right]\delta\theta \mathrm{d}V, \quad \forall\delta\theta \qquad (37)$$
$$0 = \int_{\Gamma_{0,grain}} \boldsymbol{N}\cdot\boldsymbol{P}\cdot\delta\boldsymbol{u}\mathrm{d}A - \int_{\mathcal{B}_{0,grain}} \boldsymbol{P}:\nabla_0(\delta\boldsymbol{u})\mathrm{d}V, \quad \forall\delta\boldsymbol{u}$$
$$\int_{\mathcal{B}_{0,grain}} g_\beta\delta g_\beta\mathrm{d}V = \int_{\Gamma_{0,grain}} \gamma_\beta \boldsymbol{N}\cdot\bar{\boldsymbol{s}}_\beta\mathrm{d}A - \int_{\mathcal{B}_{0,grain}} \gamma_\beta\nabla_0(\delta g_\beta)\cdot\bar{\boldsymbol{s}}_\beta\mathrm{d}V, \quad \forall\delta g_\beta.$$

The approximations of θ, $\boldsymbol{u}$ and g_β are assumed to be linear and the nonlinear coupled equations are solved in a monolithic fashion.

6. Boundary conditions

Different type of boundary conditions have to be formulated. First, mechanical boundary conditions are proposed.

6.1. Mechanical boundary conditions

We choose Dirichlet boundary conditions on the entire outer boundary Γ_0. Consequently, the boundary conditions for the specimen read as follows

$$\boldsymbol{u}(\boldsymbol{X}) = \boldsymbol{u}_0 \quad \forall \boldsymbol{X} \in \Gamma_0. \qquad (38)$$

We set the displacement field inside the grains and on the inner grain boundaries unconstrained in order to better capture the underlying physics.

6.2. Microboundary conditions

The gradient hardening boundary conditions must be defined for all the grain boundaries and not only for the outer boundary of the grain structure. In the literature, there mainly exist two types of micro boundary conditions, namely micro-hard and micro-free. The latter correspond to a vanishing microstress κ_β, whereas the first one assumes that the plastic slip γ_β vanishes on the grain boundaries:

$$\gamma_\beta = 0 \quad \text{on } \Gamma_{0,grain\,\beta} \quad \text{micro-hard b.c.} \qquad (39)$$

$$\kappa_\beta = 0 \quad \text{on } \Gamma_{0,grain\,\beta} \quad \text{micro-free b.c.} \qquad (40)$$

An additional type of boundary conditions, the micro-flexible ones, have been supplemented by Ekh et al. (2011). In comparison to the established micro-hard and micro-free conditions, the micro-flexible conditions are physically more realistic. In detail, micro-flexible boundary conditions depend on the angle of misorientation between to neighboring grains and contain the micro-hard as well as the micro-free conditions as limiting cases. Consequently, the grain boundary resistance depends on the degree of mismatch between the slip systems. The micro-hard condition corresponds to a boundary through which dislocations cannot pass, whereas the

micro-free condition corresponds to a boundary through which dislocations can flow freely without any resistance.

Grain boundaries decrease the thermal (and the electrical) conductivity, depending on the number of misfit dislocations. Therefore, it is reasonable to assume a dependence of the angle of misorientation. To be precise, micro-flexible boundary conditions (defining the relation between the plastic slip γ_β and the micro-stress $\kappa_{\Gamma,\beta}$) read as follows

$$\gamma_\beta = C_{\Gamma,\beta}(\varphi_{ab,\beta})\,\kappa_{\Gamma,\beta} \quad \text{on } \Gamma_{0,\text{grain}\,\beta} \quad \text{micro-flexible b.c.,} \tag{41}$$

with

$$C_{\Gamma,\beta}(\varphi_{ab,\beta}) := C_\Gamma \, \frac{1}{\tan(\varphi_{ab,\beta})} \tag{42}$$

where C_Γ is the flexibility constant, and $\varphi_{ab,\beta}$ is the angle of mismatch between slip direction $\bar{\boldsymbol{s}}_\beta$ in grain a and the most compatible slip direction in grain b. To be specific, the angle of mismatch $\varphi_{ab,\beta}$ is defined as

$$\varphi_{ab,\beta} = \min_\iota \{\arccos |\bar{\boldsymbol{s}}_\beta^a \cdot \bar{\boldsymbol{s}}_\iota^b|\}, \quad \iota = 1, \ldots, N_{\text{grain}}. \tag{43}$$

Note that the micro-flexible boundary condition is continuous with respect to the angle of mismatch.

6.3. Temperature boundary conditions

For the thermal problem, we assume Neumann boundary conditions on the entire boundary

$$\mathbf{Q} \cdot \mathbf{N} = 0 \quad \text{on } \Gamma_0. \tag{44}$$

Physically, this corresponds to an adiabatic boundary, i.e., a boundary that is impermeable to heat transfer.

Another possibility would be to adopt periodic boundary conditions for the thermal (as well as mechanical) problem which would be especially efficient if a representative response of the grain structure would be the main objective.

7. Numerical results

In this section we investigate the temperature fluctuation in a grain structure during fast loading. The main purposes of this section are to show how large the temperature fluctuation field might be and what magnitude the loading rate must be in order to obtain such a fluctuation field. Although the loading rate is very high we will for simplicity neglect inertia effects and assume quasi-static loading conditions (cf. Eq. (37)$_2$). The model is applied to a polycrystalline metal. The material parameters are listed in Table 1 and it is assumed that all material parameter values are independent on the temperature.[1] Clearly, the choice of parameter values should be further investigated to get more realistic results for a specific choice of material. In this paper we restrict the study to a choice of parameter values that give qualitatively realistic stress–strain response for a polycrystalline metal. However, the influence of varying the gradient hardening H_g and the relaxation time t_* is investigated. In all the numerical examples plane stress condition (in every Gauss point of the grain structure) is assumed.

---

[1] In this particular case, i.e., with the constitutive assumptions listed, Eq. (22) can be written in local form as follows

$$\rho_0 c \dot{\theta} = -\text{Div}\mathbf{Q} + \rho_0 r + \boldsymbol{\tau} : \boldsymbol{d}^p + \sum_\beta \kappa_\beta \dot{v}_\beta - \frac{3\alpha(\lambda + 2/3\,\mu)(1 - \log(J))\,\theta}{2J}(\mathbf{C}^e)^{-1} : \dot{\mathbf{C}}^e.$$

Table 1
Material parameter values adopted for the crystal gradient plasticity model. The mechanical parameters are from Ekh et al. (2011) whereas the thermal parameters are from Håkansson et al. (2008).

Parameter	Symbol	Value
Young's modulus	E	200 [GPa]
Poisson's ratio	v	0.3
Local hardening modulus	H^l	10 [GPa]
Gradient hardening modulus	H_0^g	$4 \cdot 10^4$ [GPa]
Internal length scale	l	0.01 [μm]
Initial yield stress	Y_β	1000 [MPa]
Rate sensitivity parameter	m	1
Drag stress	C_0	1 [MPa]
Heat source	r	0
Material density	ρ_0	7800 [kg/m^3]
Heat capacity	c	450 [J/kg K]
Thermal conductivity	k	30 [W/m k]
Thermal expansion coefficient	α	10^{-5} [K^{-1}]

7.1. Influence of loading rate

First, numerical results for a simple shear test for a grain structure consisting of four grains are presented. We consider this simple but illustrative example as it already clearly demonstrates first abilities of the proposed model. A maximum shear deformation of $\bar{\gamma} = 0.05$ with three different loading rates $\dot{\bar{\gamma}}$ are applied. In these results the relaxation time t_* is thought of as a regularization parameter for crystal plasticity, i.e., chosen as small as possible to give (close to) rate independent mechanical response. The particular choice of the relaxation time is therefore changed with the loading rate as $t_* = 50/\dot{\bar{\gamma}}$. The numerical results now only show rate dependence response due to different temperature fields.

The temperature field is initiated as homogeneous with $\theta = 293$ K everywhere. Furthermore, random triple slip is assumed to allow for multiple active slip systems and micro-hard conditions are assumed $C_\Gamma = 0$. The four grains are discretized with 228, 240, 264 and 292 elements. The mechanical response in terms of stress–strain curve and accumulated plastic slip field $\sqrt{\sum_\beta \gamma_\beta^2}$ are shown in Figs. 2 and 3. These results are the same independent on the loading rate (due to the adopted choice of t_*). However, if we study the increased (from 293 K) temperature field in Fig. 4 then we observe that the loading rate has a significant influence during a short time period. The lower the loading rate is the more homogeneous the temperature field becomes. For $\dot{\bar{\gamma}} = 5 \cdot 10^4$ s^{-1} the temperature field is close to homogeneous.

The relation between the plastic slip γ_β and the temperature θ is nontrivial. The more plastic slip arises, the more heat is generated.
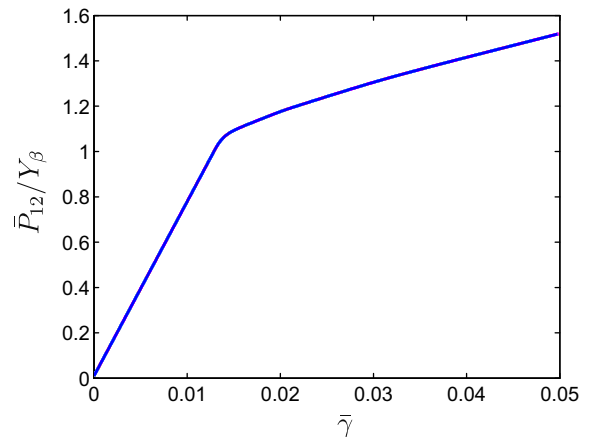

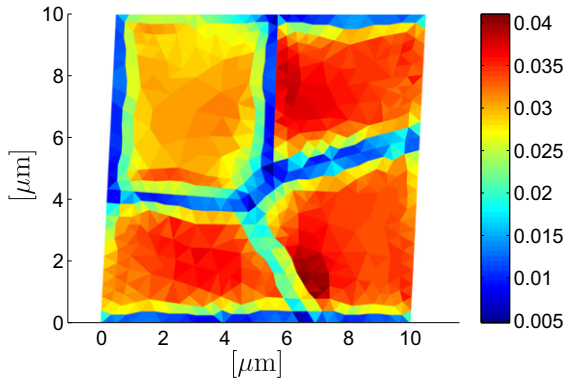**Fig. 2.** Stress strain curve for a simple shear test of 4 grains.

Fig. 3. Distribution of accumulated plastic strain in the grain structure.

Fig. 5. Stress strain curve for a simple shear test of 16 grains.

The comparison of Figs. 3 and 4 reveals that the temperature rises in the parts of the grains with the highest accumulated plastic slip. The temperature evolution happens at a different speed when compared to the speed of the plastic slip development. This finding can also be seen in the examples below.

Now we adopt the same assumptions for a larger grain structure with 16 grains. Each grain is discretized with 250–300 elements. The stress–strain curve and the accumulated plastic slip field are shown in Figs. 5 and 6 whereas the temperature fields for different loading rates are shown in Fig. 7. The same conclusions as for the four grain example can be drawn here, i.e., for the lower loading $\dot{\bar{\gamma}} = 5 \cdot 10^4 \, \text{s}^{-1}$ then the temperature field becomes close to homogeneous.

In the next results we allow also the mechanical behavior to be rate dependent. To be specific, we subject the grain structure to three different loading rates but now with the same relaxation time $t_* = 10^{-4}$ s. This means that the model's viscosity influences the mechanical response. The resulting stress–strain response for $\dot{\bar{\gamma}} = 5 \cdot 10^5$, $5 \cdot 10^6$ and $1 \cdot 10^7 \, \text{s}^{-1}$ are shown together with the plastic slip field for $\dot{\bar{\gamma}} = 5 \cdot 10^6$ in Figs. 8 and 9. From the latter result, we can compare with the plastic slip field in Fig. 6 and conclude that the plastic slip now is smaller due to the larger strain rate.

In addition, the temperature fields for the different loading rates are shown in Fig. 10. Here, we observe that a slow loading rate allows the heat to spread more in the grain structure. But also that for the highest loading rate the overall temperature raise is slightly smaller. It should be noted that if we instead would have compared the temperature distribution for the same stress level (and not strain level) then the difference between the overall temperatures would have been larger.
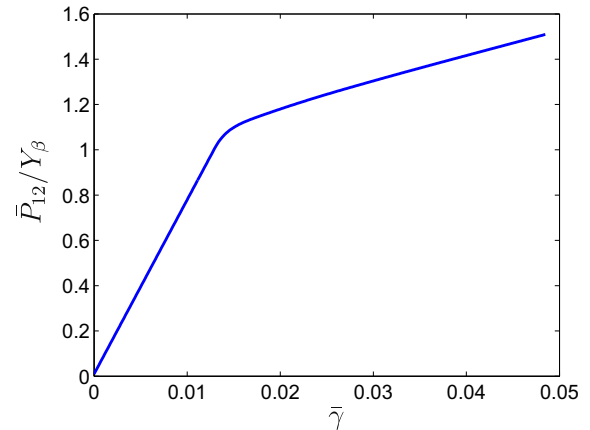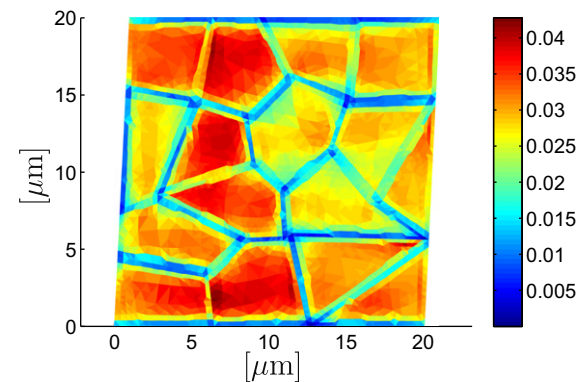

Fig. 6. Distribution of accumulated plastic strain in the grain structure.

7.2. Influence of grain size and boundary conditions

Another important model parameter is the size of the grain structure. For the 16 grain example in SubSection 7.1 the side length was assumed to be 20 μm. If we now decrease the side length to 10 μm then the gradient crystal plasticity model predicts a more stiff result. Moreover, the accumulated plastic slip field is affected by this change of hardening but also the temperature field will be affected. The accumulated plastic slip and temperature field for the side length 10 μm are shown in Fig. 11 at $\bar{\gamma} = 0.05$ for the loading rate $\dot{\bar{\gamma}} = 5 \cdot 10^5 \, \text{s}^{-1}$ and relaxation time $t_* = 10^{-4}$ s. These results should be compared to Fig. 5 and 10 (left). The width of grain boundary affected plastic slip field is similar for the two grain structures. In addition, we can observe that the smaller side length
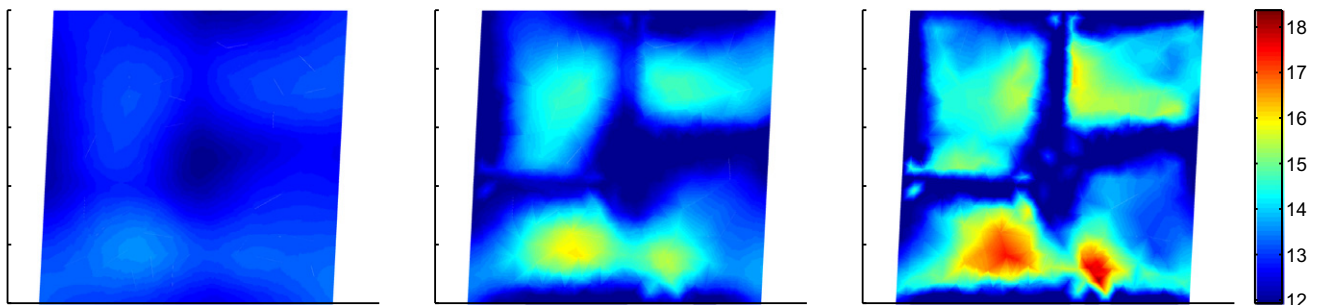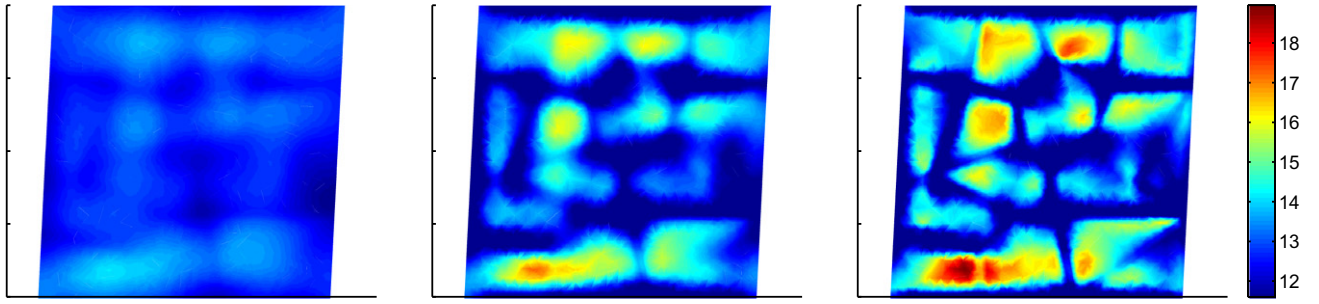

Fig. 4. Temperature distribution $\theta - 293$ K at $\bar{\gamma} = 0.05$ for, from left to right, $\dot{\bar{\gamma}} = 5 \cdot 10^4 \, \text{s}^{-1}$, $\dot{\bar{\gamma}} = 5 \cdot 10^5 \, \text{s}^{-1}$ and $\dot{\bar{\gamma}} = 5 \cdot 10^6 \, \text{s}^{-1}$, respectively.
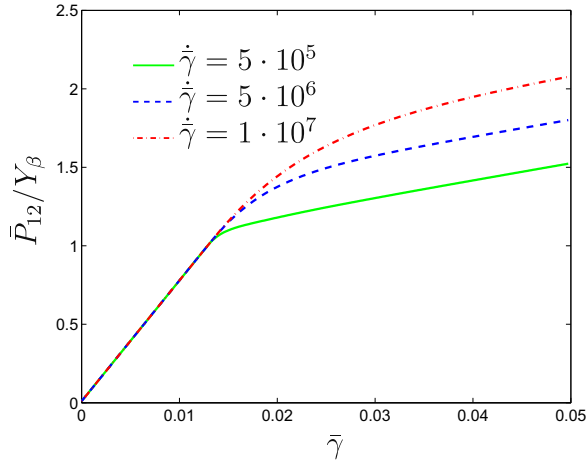
Fig. 7. Temperature distribution $\theta - 293$ K at $\bar{\gamma} = 0.05$ for, from left to right, $\dot{\bar{\gamma}} = 5 \cdot 10^4$ s^{-1}, $\dot{\bar{\gamma}} = 5 \cdot 10^5$ s^{-1} and $\dot{\bar{\gamma}} = 5 \cdot 10^6$ s^{-1}, respectively.
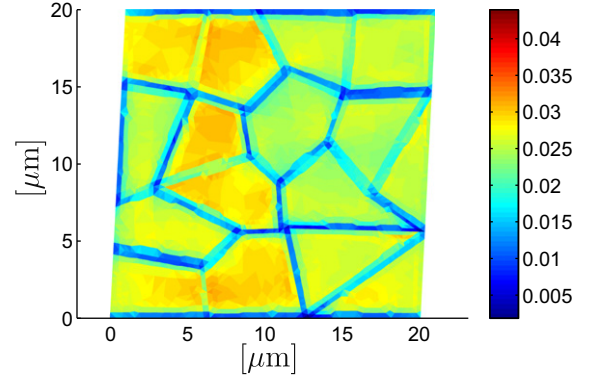

Fig. 9. Distribution of accumulated plastic strain in the grain structure for the loading rate $\dot{\bar{\gamma}} = 5 \cdot 10^6$ s^{-1}.
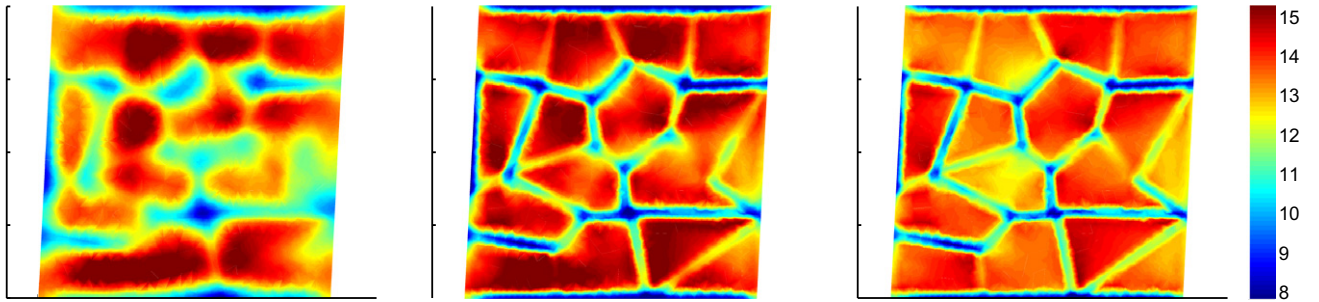
Fig. 8. Stress strain curves for a simple shear tests with different loading rates of grain structure with 16 grains.

Fig. 10. Temperature distribution $\theta - 293$ K at $\bar{\gamma} = 0.05$ for, from left to right, $\dot{\bar{\gamma}} = 5 \cdot 10^5$ s^{-1}, $\dot{\bar{\gamma}} = 5 \cdot 10^6$ s^{-1} and $\dot{\bar{\gamma}} = 1 \cdot 10^7$ s^{-1}, respectively.
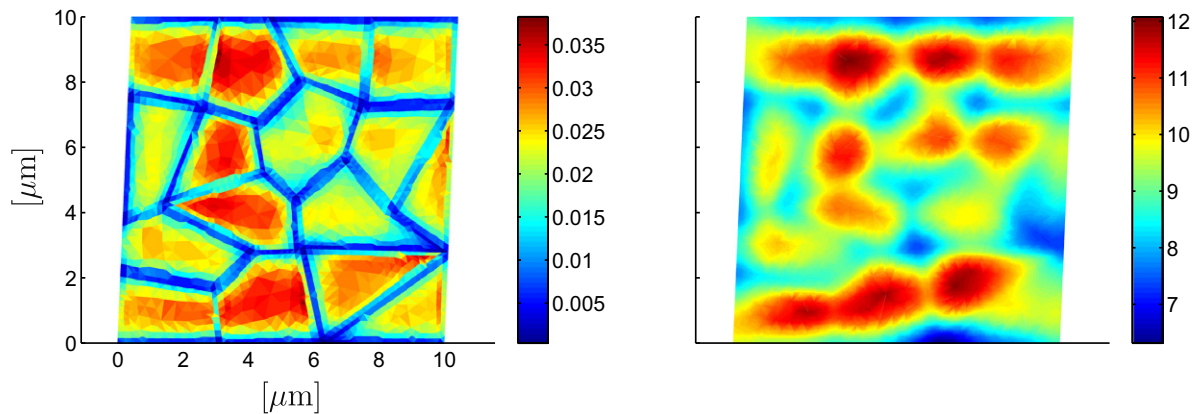

Fig. 11. Left: accumulated plastic slip and Right: temperature distribution $\theta = 293$ K at $\bar{\gamma} = 0.05$ for the side length of the grain structure 10 μm.
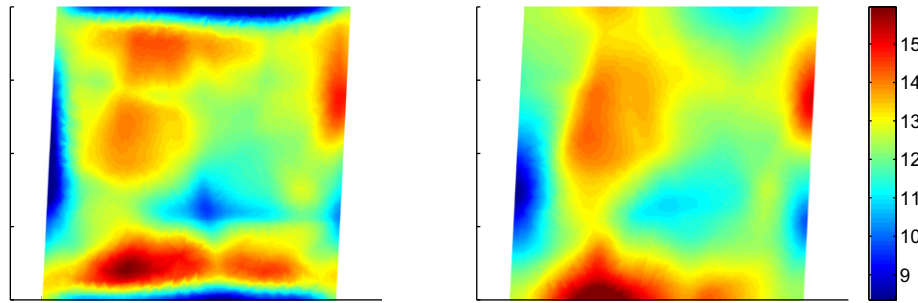
Fig. 12. Temperature distribution $\theta - 293$ K at $\bar{\gamma} = 0.05$ for; Left: microflexible $C_\Gamma = 1$ μm/N inner boundaries and microclamped outer boundaries, Right: micro-free boundary conditions.

gives a slightly more homogeneous temperature distribution with lower maximum temperature.

Finally, we investigate the influence of the boundary conditions on the plastic slip field as discussed in Section 6. In Fig. 12 the temperature fields for micro-free $C_\Gamma = \infty$ (in the computer implementation the finite value $C_\Gamma = 10^6$ μm/N is chosen) and microflexible $C_\Gamma = 1$ μm/N at $\bar{\gamma} = 0.05$ conditions at inner grain boundaries are shown. It can be observed that, by comparing to Fig. 10 (left), that the temperature distribution now becomes more homogeneous.

8. Concluding remarks

We extended our non-local, geometrically nonlinear crystal plasticity framework by taking heat conduction into account. The governing equations were derived in thermodynamically consistent framework and include couplings between the mechanical and the thermal problem. Moreover, the phenomenological flow law for the plastic slip (Eq. (32)) is temperature-dependent via the constitutive equation for the Kirchhoff stress tensor $\boldsymbol{\tau}$ as stated in Eq. $(25)_1$. Moreover, changes in the temperature field influence the deformation field and vice versa, i.e., the coupling is twofold. The temperature development inside the grain depends on the active slip systems and, therefore, on the slip directions, see Eq. (22). Consequently, some grains are better orientated for heat generated by plasticity than others, in other words heat will distribute differently in grains with different preferred slip directions.

The numerical algorithm is based on a domain decomposition where in each grain the coupled field equations for the displacements, temperatures and the gradient hardening are solved for in a monolithic fashion. This is done for given displacements and temperatures on the grain boundaries. These displacements and temperatures are solved in the outer global problem. In order to take the two-folded coupling of the balance of linear momentum and the heat equation fully into account, we solve the system of equations monolithically with the help of the Newton–Raphson solution strategy. The numerically efficient finite element algorithm is suitable for parallelization as this is relevant for polycrystalline examples.

The work presented in this paper contributes to the ongoing research direction on extended crystal plasticity theories, suggesting a way on how to consider the coupled thermomechanical problem. Different aspects of the response of polycrystalline specimen have been studied. The influence of the loading rate on the temperature field in a polycrystalline model has been studied. It is concluded that for high strain rates $\sim 10^5$ s^{-1} and grain sizes ~ 10 μm the temperature becomes clearly inhomogeneous. In engineering many metals are used (e.g., casted metals) with larger grain sizes whereby the significance of the inhomogeneous temperature field is of importance for lower strain rates. Finally, for the same polycrystalline model different boundary conditions on the plastic slip have been adopted and results showing their influence have been shown.

References

Al-Rub, R.K.A., Faruk, A.N.M., 2011. Coupled interfacial energy and temperature effects on size-dependent yield strength and strain hardening of small metallic volumes. Journal of Engineering Materials and Technology 133, 0110171–0110177.

Anand, L., Gurtin, M.E., Lele, S.P., Gething, C., 2005. A one-dimensional theory of strain-gradient plasticity: formulation, analysis, numerical results. Journal of the Mechanics and Physics of Solids 53, 1789–1826.

Asaro, R., 1983. Crystal plasticity. Journal of Applied Mechanics ASME 50, 921–934.

Bargmann, S., Svendsen, B., Ekh, M., 2011. An extended crystal plasticity model for latent hardening in polycrystals. Computational Mechanics 48, 631–645.

Cermelli, P., Gurtin, M.E., 2001. On the characterization of the gemetrically necessary dislocations in finite plasticity. Journal of the Mechanics and Physics of Solids 49, 1539–1568.

Ekh, M., Grymer, M., Runesson, K., Svedberg, T., 2007. Gradient crystal plasticity as part of the computational modeling of polycrystals. International Journal for Numerical Methods in Engineering 72, 197–220.

Ekh, M., Bargmann, S., Grymer, M., 2011. Influence of grain boundary conditions on modeling of size-dependence in polycrystals. Acta Mechanica 218, 103–113.

Evers, L.P., Brekelmans, W.A.M., Geers, M.G.D., 2004. Scale dependent crystal plasticity framework with dislocation density and grain boundary effects. International Journal of Solids and Structures 41, 5209–5230.

Gurtin, M.E., 2000. On the plasticity of single crystals: free energy, microforces, plastic-strain gradients. Journal of the Mechanics and Physics of Solids 48, 989–1036.

Håkansson, P., Wallin, M., Ristinmaa, M., 2008. Prediction of stored energy in polycrystalline materials during cyclic loading. International Journal of Solids and Structures 45, 1570–1586.

Hill, R., 1966. Generalized constitutive relations for incremental deformation of metal crystals by multislip. Journal of the Mechanics and Physics of Solids 14, 95–102.

Kröner, E., 1960. Allgemeine Kontinuumstheorie der Versetzungen und Eigenspannungen. Archive for Rational Mechanics and Analysis 4, 273–334.

Lee, E.H., 1969. Elastic–plastic deformation at finite strains. Journal of Applied Mechanics 36, 1–6.

Nemat-Nasser, S., Guo, W.-G., Kihl, D., 2001. Thermomechanical response of AL-6XN stainless steel over a wide range of strain rates and temperatures. Journal of the Mechanics and Physics of Solids 49, 1823–1846.

Rice, J., 1971. Inelastic constitutive relations for solids: an internal-variable theory and its application to metal plasticity. Journal of the Mechanics and Physics of Solids 19, 433–455.

Svedberg, T., Runesson, K., 1998. An algorithm for gradient-regularized plasticity coupled to damage based on a dual mixed FE-formulation. Computer Methods for Applied Mechanics and Engineering 161, 49–65.

Svendsen, B., Bargmann, S., 2010. On the continuum thermodynamic rate variational formulation of models for extended crystal plasticity at large deformation. Journal of the Mechanics and Physics of Solids 58, 1253–1271.

Voyiadjis, G.Z., Beliktas, F.H., 2005. Microstructural based models for bcc and fcc metals with temperature and strain rate dependency. Mechanics of Materials 37, 355–378.

Zhou, M., Clode, M.P., 1998. Constitutive equations for modelling flow softening due to dynamic recovery and heat generation during plastic deformation. Mechanics of Materials 27, 63–76.